GEOPHYSICS, VOL. 81, NO. 1 (JANUARY-FEBRUARY 2016); P. WA147–WA157, 13 FIGS.
10.1190/GEO2015-0157.1

Multidisciplinary geophysical investigations over an alpine rock glacier

Kaspar Merz[1], Hansruedi Maurer[1], Lasse Rabenstein[1], Thomas Buchli[2], Sarah M. Springman[2], and Matthias Zweifel[1]

ABSTRACT

We have performed a multidisciplinary geophysical survey combined with geotechnical investigations over a degrading alpine rock glacier. A dense grid of helicopter-borne ground-penetrating radar data allowed the 3D shape of the bedrock topography and the gross transition from ice-rich to ice-poor parts of the rock glacier to be delineated. The bedrock topography served as a 2D structural constraint for tomographic inversions of seismic and geoelectric data acquired on coincident profiles parallel and perpendicular to the rock glacier flow direction. These profile data were complemented by a small 3D geoelectric tomography experiment. Only a combined interpretation of all the results allowed reliable and unambiguous interpretation of the tomograms. We could distinguish between the active layer, bedrock, ice-bearing rock glacier material, and degraded permafrost within the rock glacier. The latter could be further distinguished in areas where the ice must have melted only recently, and regions that had degraded some time ago. Additionally, high-resolution cross-hole radar tomography, performed in an area of opening crevices, allowed small-scale structures to be resolved, which were indicative of the dominant deformation mechanisms style of the rock glacier. The success of our study was primarily based on the availability of 3D data sets that allowed important structures to be traced over larger areas and the integrated interpretation of several data types. We have identified the internal structure of the rock glacier to be surprisingly heterogeneous with several small-scale features that were judged to be critical for assessing its stability. This underpinned the need for comprehensive 3D structural investigations to augment geotechnical measurements linearly with inclinometers or at points in boreholes.

INTRODUCTION

Global climate change is estimated to have a larger impact on sensitive circumpolar and mountainous cryogenic regions than in other regions (e.g., Harris et al., 2009). This temperature increase affects primarily permafrost, which is defined as soil at or below 0°C for two or more consecutive years. Rock glaciers are particular expressions of ice-rich mountain permafrost at high altitudes in lower latitude regions. These large tongue- or lobate-shaped bodies range from accumulations of angular boulders and debris cemented together by ice to masses of nearly pure ice overlain by layers of boulders and debris (e.g., Burger et al., 1999) and show signs of deformation at the surface. They creep down mountain slopes at rates of 0.01–5.0 m/yr when active (Whalley and Martin, 1992; Springman et al., 2012). It is estimated that they are responsible for approximately 20% of all mass transport in such terrains (Barsch, 1996). Because substantial regions of many rock glaciers are just below the melting point, they are sensitive to relatively small increases in mean annual temperature. Subtle temperature increases can cause the ice to melt, resulting in higher creep rates, instabilities, and potentially even catastrophic mass movements (e.g., Crosta et al., 2004; Krysiecki et al., 2008).

Rock glaciers are therefore a potential natural hazard in populated mountain areas. For modeling and predicting movement rates, the physical properties and the thermohydromechanical characteristics of these important permafrost structures need to be known.

Manuscript received by the Editor 9 March 2015; revised manuscript received 20 June 2015; published online 21 December 2015; corrected version published online 7 January 2016.
[1]ETH Zurich, Institute of Geophysics, Zurich, Switzerland. E-mail: kaspar.merz@erdw.ethz.ch; hansruedi.maurer@erdw.ethz.ch; lasse.rabenstein@erdw.ethz.ch; mzweifel@gmx.ch.
[2]ETH Zurich, Institute for Geotechnical Engineering, Zurich, Switzerland. E-mail: thomas.buchli@igt.baug.ethz.ch; sarah.springman@igt.baug.ethz.ch.

Geotechnical investigations are one possible option. Mechanical and hydraulic parameters can be estimated either on selected samples in the laboratory or with in situ tests in the field (e.g., Springman et al., 2012). Such geotechnical data provide information only linearly (inclinometers) or at one point. By contrast, geophysical investigations, sensitive to different sets of parameters, allow larger subsurface volumes to be probed in a nondestructive manner, and therefore they represent an attractive option to complement geotechnical measurements.

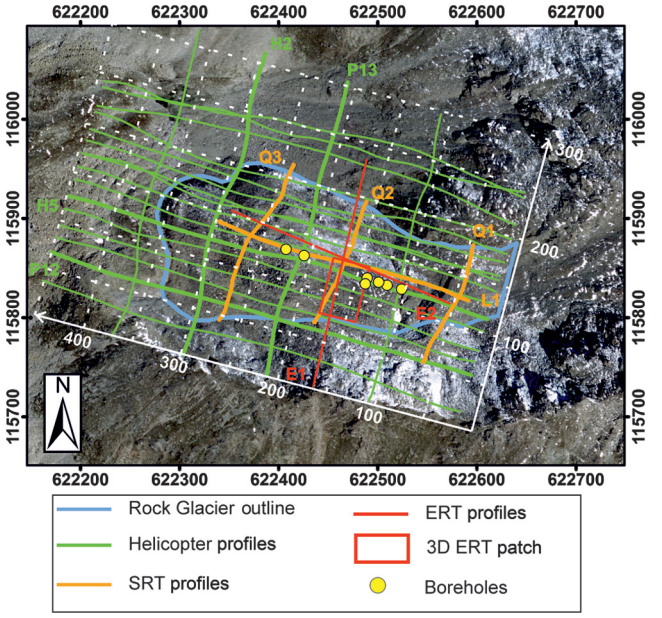

Figure 1. Map of the Furggwanghorn study site. The outline of the rock glacier is shown in blue. Green, orange, and red lines show the locations of the helicopter GPR, SRT, and ERT surveys, respectively. The boreholes are marked by yellow dots. Black coordinates at the outside of the map are in the Swiss coordinate system CH1903 (geodata: Swisstopo). A local coordinate system, shown in white and in meters, is superimposed.

During the past several years, numerous studies have been devoted to geophysical characterization of rock glaciers. Good overviews on the possibilities and limitations of such surveys can be found in Maurer and Hauck (2007) and Kneisel et al. (2008). In brief, seismic refraction tomography (SRT) (e.g., Musil et al., 2002), ground-penetrating radar (GPR) (e.g., Monnier et al., 2011), and geoelectrics (e.g., Hauck et al., 2003) have proved to be the most effective methods. Furthermore, it has been shown that multidisciplinary investigations, in which several geophysical methods were combined with geotechnical measurements, were especially beneficial (e.g., Maurer and Hauck, 2007).

Nearly all geophysical investigations on rock glaciers have indicated a high degree of subsurface heterogeneity (Musil et al., 2002; Hausmann et al., 2012). Therefore, the question arises as to whether the results from single 2D profile data correctly portray the physical properties within the vertical cross section beneath the profile, or if out-of-plane effects could be significant. To fully address this problem, it would be necessary to perform 3D surveys. Such investigations have not yet been performed because geophysical data acquisition in high alpine areas can be extremely challenging, particularly on highly heterogeneous rock glacier terrain

In this contribution, we present results from a multidisciplinary project on a rock glacier located in the western Swiss Alps. This study is distinguished from previous ones by the availability of 3D GPR and geoelectric data sets. These data are complemented by 2D results from SRT and high-resolution crosshole GPR tomography. In combination with results from extensive geotechnical measurements, these unique data sets offered an excellent opportunity to characterize the rock glacier. After a short introduction to the test site, we demonstrate how critical features, such as bedrock topography, the presence of ice, and zones of particularly strong degradation, can be delineated reliably by combining the information content offered by all the available data sets.

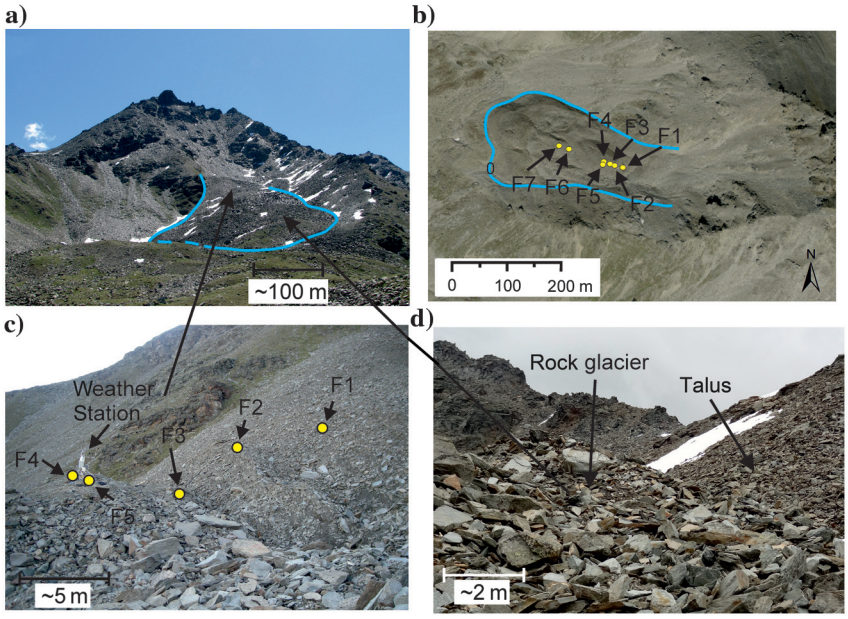

Figure 2. Photographs of the study site. (a) Frontal view of the Furggwanghorn rock glacier. Its outline is marked in blue. (b) Orthophoto of the rock glacier. The blue line marks the outline of the active rock glacier. (c) Yellow dots show the locations of the boreholes F1–F7 close up of the depressions with the locations of the boreholes F1–F5 and the weather station. In the foreground, the boulder-covered surface is visible. (d) Blocky surface in the central part of the rock glacier and the talus slope at its southern boundary.

STUDY SITE

Our study site, the Furggwanghorn rock glacier, lies in the western Swiss Alps at altitudes between 2750 and 2900 m asl (Figures 1, 2a, and 2b). The geology is part of the crystalline alpine nappes and consists mainly of schist and gneisses (Buchli et al., 2013; Swisstopo, 2015). Weathering of these rocks has produced material in the size range from silt to angular-shaped blocks of up to 2 m in diameter (see Figure 2d). The source of all rock glacier material is talus originating from the surrounding alpine peaks and slopes (Figure 2a). The rock glacier is close to the lower thermal permafrost boundary, as described in Boeckli et al. (2012). Therefore, temperatures in the permafrost are expected to be close to 0°C. Deformation measurements

based on the analysis of aerial imagery show increasing movement rates of up to 1.5 m/yr over several years (Kääb et al., 2007; Roer et al., 2008), which have recently accelerated to 3 m/yr (Buchli et al., 2013). Kääb et al. (2007) suggest that the increase in movement rates is related to increasing mean annual surface temperatures in the region. As a result of these large movements, deep surface depressions have formed near the root zone on the rock glacier, as shown in Figure 2c. To investigate the thermal conditions of the rock glacier and to monitor deformation at depth, seven boreholes were drilled to a depth of 25 m (F1–F5) and 28 m (F6–F7) through the active layer and the top part of the rock glacier. Inclinometers installed in three of these boreholes (F5, F6, and F7) showed that the deformations continued over the recent years, and the rates have increased up to 4 m/yr in some areas of the rock glacier (Buchli et al., 2013). This indicates an accelerated movement in the last few years. The inclinometer measurements show a shear zone to be present at a depth of approximately 15 m in the top part of the rock glacier (Buchli et al., 2013) and at 18–20 m depth in its lowermost part in boreholes F6 and F7 (Figure 2b).

HELICOPTER-BORNE GPR

GPR has proven to be very effective for investigating the internal structures of rock glaciers (Lehmann and Green, 2000; Berthling et al., 2008; Monnier et al., 2011; Krainer et al., 2012; Monnier and Kinnard, 2013; Florentine et al., 2014). So far, most studies have used ground-based GPR systems, but difficult access to very steep parts of the rock glacier and wave scattering on large boulders in close vicinity of the antennas have caused GPR signals to be distorted (Musil et al., 2002; Merz et al., 2015a).

Airborne GPR systems overcome these two main problems. The literature includes numerous impressive examples of helicopter-borne GPR (H-GPR) surveys performed on alpine ice glaciers and ice sheets (e.g., Arcone, 2002; Rutishauser et al., 2015). This motivated us to apply this technique on the Furggwanghorn rock glacier. We acquired 20 lines of H-GPR data in spring 2012, out of which 16 lines were oriented along and four lines perpendicular to the main flow direction of the rock glacier (Figure 1). A 60-MHz GSII GPR system was used, with the antennas mounted directly on the helicopter skids. The flight height was 10–15 m above ground. More details on the data acquisition and data processing can be found in Merz et al. (2015a, 2015b).

As an example of the results, Figure 3a shows the processed section for H-GPR profile H5 (see Figure 1 for its location). The bedrock interface can be easily recognized in the data, indicated by the white arrows in Figure 3a. Most other profiles exhibit similarly good bedrock reflections, and there is an excellent correlation of this feature in adjacent profiles (Merz et al., 2015a). Similarly, reflector *r* in Figure 3a can be traced in neighboring profiles. This allowed the approximate location of this reflector to be delineated, and it was found that it must be located within the bedrock underneath the rock glacier (see also Merz et al., 2015b). The relatively large number of H-GPR profiles acquired allowed the 3D shape of the bedrock topography to be determined, which is shown with the green surface in Figure 3b. It is bowl-shaped and at a maximum depth of 48 m in the central part of the rock glacier. The overall volume of the rock glacier was estimated to be 910,000 m^3 on the basis of the H-GPR data.

In addition to yielding information on the bedrock topography, the H-GPR sections exhibit a change in the reflectivity characteristics at approximately 20 m depth. As with the bedrock reflections, this feature can be traced across most profiles, and it is indicated with the magenta lines in Figure 3b.

HELICOPTER-BORNE GPR CONSTRAINED SEISMIC REFRACTION TOMOGRAPHY

Seismic methods have been used in several rock glacier studies to delineate bedrock topography (e.g., Musil et al., 2002; Ikeda, 2006; Hausmann et al., 2012), but strong scattering from heterogeneous subsurface structures made it difficult to image seismic reflections (Musil et al., 2002). By contrast, SRT (e.g., Lanz et al., 1998) proved to be a feasible option. The gross internal structures could also be imaged (e.g., Maurer and Hauck, 2007), as well as bedrock topography. Typically, rock glaciers consist of a surface layer with low seismic velocities in the range of 500–1500 m/s over a very heterogeneous zone with intermediate velocities of approximately

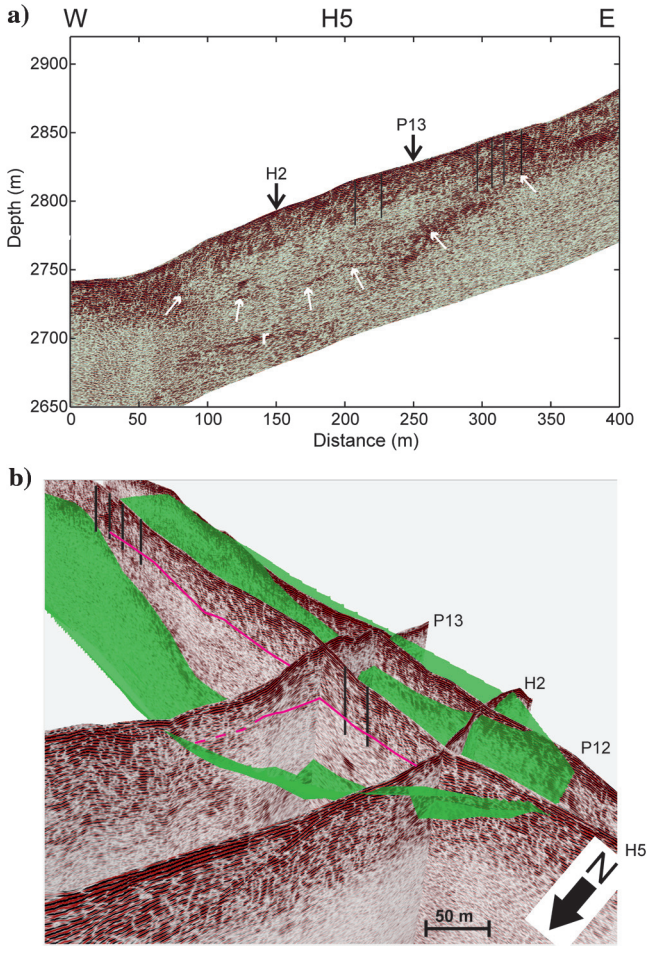

Figure 3. (a) Helicopter GPR profile H5. Topography is taken into account in the display. Crossing points of profiles H3 and P13 are marked by arrows. Locations of the boreholes are shown with black lines. White arrows point to the interpreted basement reflector. *r*: reflective basement structure. (b) Fence diagram of helicopter GPR profiles H2, H5, P12, and P13 (see Figure 1 for locations). The interpreted basement surface is shown as a green surface, the boundary between a high-reflectivity and a low-reflectivity zone is marked in magenta.

3000–4000 m/s. High velocities >4500 m/s are indicative for bedrock.

Four seismic lines were acquired on the Furggwanghorn rock glacier in spring 2010 and 2011 (Figure 1). At the time of the survey, the rock glacier was covered by 1–2 m of snow. Geophones were placed every 2 m, directly in the snow to ensure good coupling to the ground, and explosive charges of 200–400 g were fired under the snow cover (average shot spacing was 4 m). The data quality was good and allowed the first-arriving waves ("first breaks") to be picked with an accuracy better than 2 ms.

SRT is known to be ambiguous; that is, there are typically many models that can explain the data equally well. Therefore, SRT inversions have to be constrained by regularization that is typically supplied in the form of damping and smoothing (e.g., Maurer et al., 1998). Damping constraints keep the velocity models close to the initial (first-guess) model, unless deviations are demanded by the data. Smoothing constraints minimize the structural complexity within the tomograms, but they have the undesired effect that sharp interfaces may appear overly blurred in the tomograms.

Results from the H-GPR data offer powerful constraints for addressing some of these problems related with SRT. We constructed an initial seismic velocity model based on the bedrock topography obtained with the H-GPR data. Figure 4 shows the initial velocity distributions of the four seismic profiles. The initial velocity distributions within the rock glacier body and the underlying bedrock include vertical gradients that were determined by trial and error to match the observed first-break traveltimes. Because of the damping constraints, it is expected that the discontinuity in the initial models in Figure 4 should persist, if the bedrock interfaces determined with H-GPR and SRT are compatible.

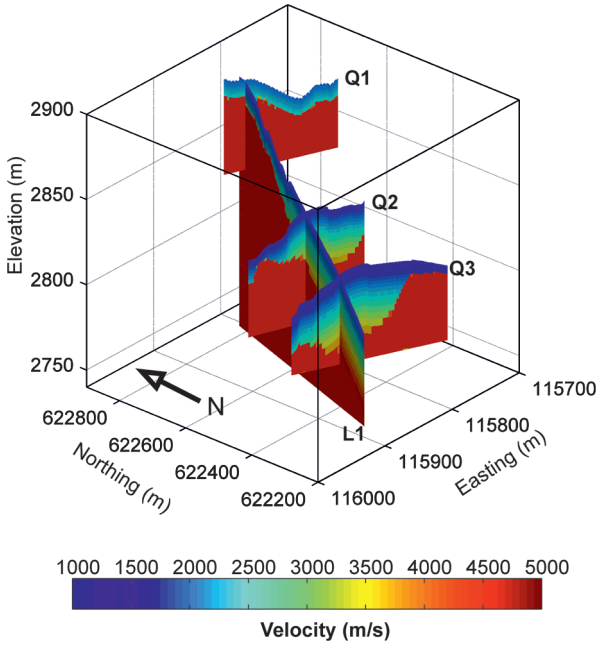

Figure 4. Fence diagram of the initial models for the four SRT inversion planes. The topography of the basement was extracted from the H-GPR data.

All the inversions converged such that the average data misfit between observed and predicted data was comparable with the first-break reading accuracy (approximately 2 ms), and the final to-

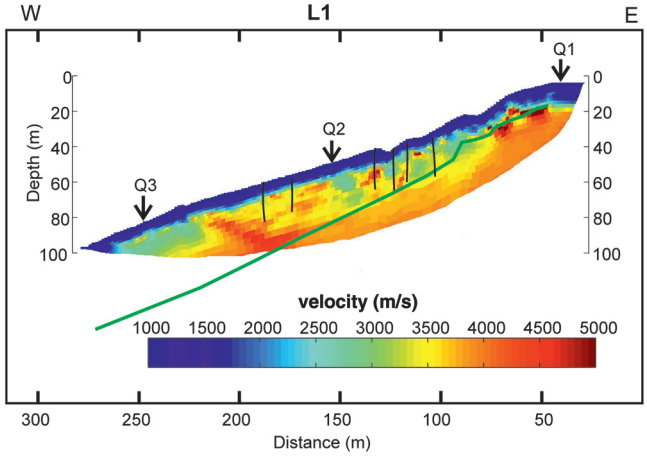

Figure 5. Final tomogram of seismic line L1 along the main flow direction of the rock glacier. The solid green line shows the depth of the bedrock extracted from the H-GPR. Black arrows at the top of the profile indicate crossing points with cross profiles Q1–Q3.

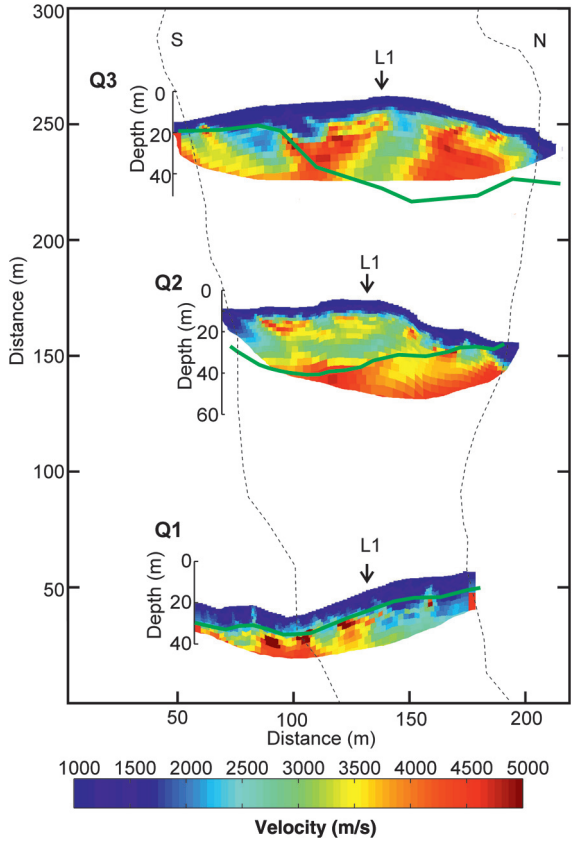

Figure 6. Final tomograms for seismic lines Q3 (top), Q2 (center), and Q3 (bottom) across the rock glacier (see Figure 1 for locations). The green lines indicate the depth of the bedrock extracted from the H-GPR. The rock glacier outline is shown as the dashed lines.

mograms are shown in Figures 5 and 6. The bedrock interface, defined by the H-GPR data, is indicated with solid green lines. In the upper part of the rock glacier (profiles Q1, Q2, and upper part of L1), there is a good consistency between the bedrock depths determined by H-GPR and SRT; that is, the seismic velocity discontinuity of the initial models was largely retained. Although profile Q1 is slightly outside of the area covered by H-GPR bedrock picks, it is evident that linear extrapolation of the H-GPR reflector toward Q1 would result in a close match of the bedrock depths.

There is no obvious correlation in the lower part of the rock glacier (west of profile Q2) between the bedrock depth determined with H-GPR and the seismic velocity structure. Profile L1 shows high velocities between 4500 and 5500 m/s from shallow depths down to the bottom of the resolved area of the SRT tomogram, and Q3 exhibits two large high-velocity bodies embedded in lower velocity material. The complex structure of the Q3 tomogram is indicative of strong lateral velocity variations, and it must be expected that significant 3D effects (i.e., seismic rays traveling partially outside of the tomographic plane) could have corrupted the SRT results. However, it is unlikely that all the discrepancies between the H-GPR and SRT results can be explained exclusively in terms of 3D effects.

HELICOPTER-BORNE GPR CONSTRAINED ELECTRICAL RESISTIVITY TOMOGRAPHY

Although the generally very resistive ground conditions on rock glaciers make electrical resistivity tomography (ERT) surveying a challenging task, several successful field studies have been reported in the literature (e.g., Hauck et al., 2003; Krautblatter et al., 2010). In particular, ERT investigations on permafrost proved to be useful for determining the ice content in the subsurface. Major problems encountered included the high contact resistance of the electrodes (i.e., poor coupling) and the consequent low level of current that could be injected into the ground. Only electrode configurations with low geometric factors could be considered due to the high contact resistance of the electrodes with blocky surface and the low amount of current that could be injected onto the ground (Hauck et al., 2003).

Two 2D ERT lines were acquired in summer 2011 along and perpendicular to the main flow direction of the rock glacier (E2 and E1 in Figure 1). We used a Syscal Pro resistivity meter with a 96 channel Syscal Pro Switch box and 2.5-m electrode spacing, resulting in a profile length of approximately 230 m. The number of data points recorded was 1485 using the Wenner configuration and 1977 using the dipole-dipole configuration. To improve coupling to the ground, the electrodes were affixed with saltwater-soaked sponges between boulders or bentonite clay was placed around them. Extensive quality checks indicated that only approximately 1200 Wenner configurations yielded reliable results.

In addition to the 2D lines, a small-scale 3D survey was carried out on the rock glacier (red frame in Figure 1). The layout included a 12×8 electrode grid covering an area of 55×45 m^2. With this deployment, we acquired a variety of different configurations including Wenner, dipole-dipole, and gradient-type measurements. Only approximately 4400 out of the total 8888 recorded configurations proved to be usable.

ERT data were inverted with the software package BERT (Günther et al., 2006; Rucker et al., 2006). Regularization of the inverse problem is critical, and it was applied in the form of smoothing constraints due of the ambiguous nature of potential field data. This resulted in unrealistically smooth subsurface images devoid of sharp boundaries, as would be expected at the bedrock interface. In a similar manner to the SRT analyses, we used the bedrock topography determined with H-GPR as an a priori constraint. Günther and Rücker (2006) show that such constraints can be implemented by decoupling the smoothing constraints across known discontinuities. Because we had no prior knowledge of the resistivities of the bedrock and rock glacier materials, we used homogeneous-resistivity starting models using the average apparent resistivities as the true resistivity values. To test the influence of the structural constraints on the inversion result, we varied the bedrock depth in the initial models within a reasonable range (not shown). In all resulting tomograms, the dominant near-surface features were very similar.

All inversions successfully converged after six iterations. Results for profiles E1 and E2 are shown in Figure 7. We observe generally higher resistivities and more structural complexity within the rock glacier body compared with the relatively uniform bedrock values. At shallow depths, there are numerous small-scale patches of increased and decreased resistivities, and within the uppermost 20 m, the resistivities are generally higher, compared with deeper parts of the rock glacier.

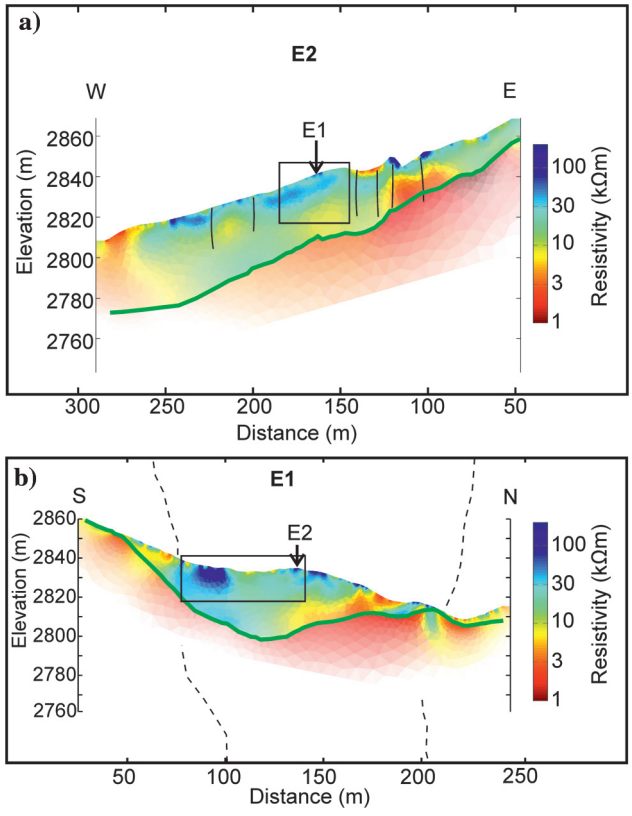

Figure 7. Resistivity tomograms derived from the two ERT lines (see Figure 1 for the location): (a) east–west profile E2 and (b) north–south profile E1. Green lines indicate the depth of the basement extracted from the helicopter GPR. This depth was used as the structural constraint in the inversion process. Black boxes mark the location and depth extension of the 3D ERT survey.

A conspicuously large high-resistivity anomaly is found in the cross profile E1 at a profile distance position of approximately 90 m. Because this anomaly lies within the area covered by the 3D ERT survey (Figure 8), it was possible to investigate the 3D extension of this feature. As shown in the 3D resistivity tomogram in Figure 8, this prominent feature extends a few tens of meters to the north (i.e., opposite to the rock glacier flow direction), and it reaches the southern border of the 3D ERT surveying area. Therefore, it is highly likely that it continues further south (i.e., in the direction of the rock glacier flow).

GPR CROSSHOLE TOMOGRAPHY

Crosshole GPR allows small-scale structures within rock glaciers to be imaged in great detail, as shown by Musil et al. (2006). We acquired three planes of crosshole data between the four collinear boreholes F1–F4 in the upper part of the rock glacier (Figures 1 and 2c). For that purpose, we used a pair of Mala 250-MHz borehole antennas. We used a semireciprocal measuring scheme to achieve a dense spatial sampling in an efficient manner. For each tomographic plane, one of the antennas was positioned at large increments of 1.0 m, and in the other borehole, the antenna was moved in small increments of 0.2 m. After completion of this setup, the procedure was repeated by interchanging large and small increments between the boreholes. Due to the pronounced surface topography between the boreholes, the first arrivals of the shallow source-receiver pairs included waves traveling through the air, and identification of the ground wave was not possible. Therefore, the ray coverage in the uppermost regions was decreased compared with the deeper parts of the tomographic planes, where the ray coverage was very good.

The tomographic inversions of the traveltimes required the borehole trajectories to be known accurately. Precise determination of the borehole collars was achieved easily with differential GPS, but determining the exact downhole shape of the boreholes was problematic. Consequently, we included the borehole trajectories as additional unknowns to be determined in the inversion problem. Maurer and Green (1997) demonstrate that it is possible to invert simultaneously for velocities and borehole coordinates. Here, we followed a slightly different strategy, as described in Maurer and Green (1997). Instead of inverting for individual transmitter and receiver positions, we parameterized the boreholes with low-order polynomials and inverted for the polynomial coefficients. After some experimentation, we found polynomials of 2° to be adequate.

The 13,693 traveltimes obtained in total from all three tomographic planes connecting the essentially colinear boreholes were inverted simultaneously to form one single tomogram. The data misfit for the final inverted model was comparable with the estimated reading accuracy (approximately 1.5 ns). The results are displayed in Figure 9. Generally, the tomograms exhibit a high degree of complexity. At shallow depths down to approximately 15 m below the surface, we observe the highest velocities. Below this depth, decreased velocities are found, particularly in the eastern part of the tomogram. The low-velocity zone is underlain by intermediate velocities, which is most pronounced in the western part of the section.

INTERPRETATION

The geophysical data sets acquired on the Furggwanghorn rock glacier revealed pronounced variations in the different physical properties. Interpreting the individual physical properties in terms of geologic, geotechnical, and glaciological units is not straightforward because the different physical parameters cannot generally be associated unambiguously with a particular unit. The only exception is the bedrock, the topography of which was constrained by the H-GPR data (Figure 3). This is also the only data set that allows a large-scale 3D interpretation to be performed. Therefore, we judged it to be appropriate to use this important and faithfully delineated interface as a regularization constraint for the SRT and ERT inversions. Identification of all remaining features requires several data sets to be interpreted jointly.

Figure 10 shows results of the approximately coincident H-GPR line H5, the seismic profile L1 and the ERT profile E2; they are located in the central part of the study area along the flow direction of the rock glacier. Superimposed on the individual cross sections is the bedrock topography shown by the green lines, as determined by H-GPR data. Note that the depths were extracted from the 3D model

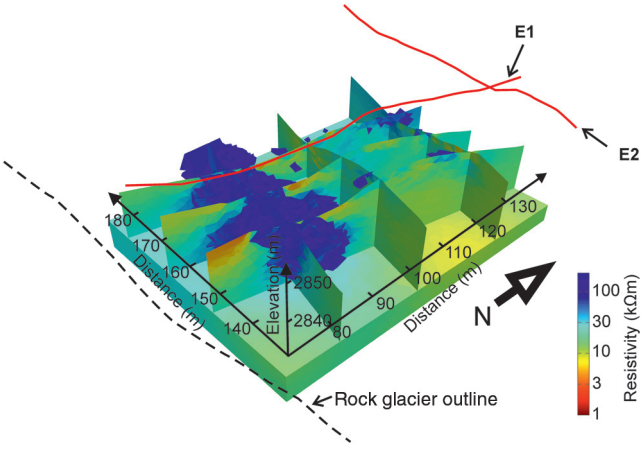

Figure 8. Slices through the inverted 3D resistivity volume. Boundaries of the blue volumes are 40 kΩm isosurfaces extracted from the volume. Red lines mark the locations of ERT profiles E1 and E2, and the dashed black line shows the rock glacier boundary.

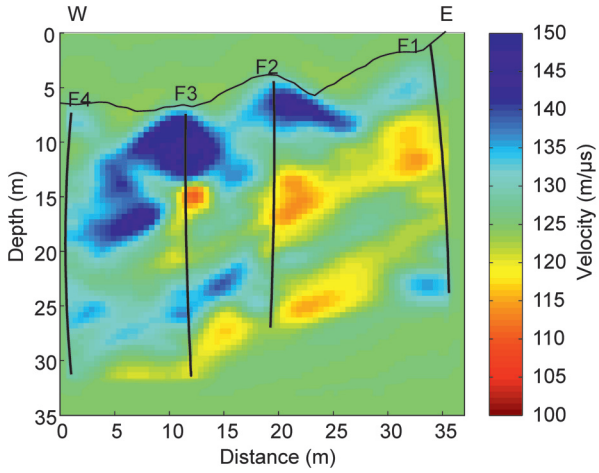

Figure 9. Radar velocity tomogram for the composite plane F1–F4. The inverted borehole trajectories are shown in black.

shown in Figure 3. The small deviations within the individual panels are due to the slightly different profile orientations.

We base our interpretation of reflectivity characteristics observed in the H-GPR data (purple lines in Figures 3 and 10) primarily on the ground-truth information from the borehole logs (Buchli et al., 2013). The structural heterogeneity that causes this change in reflectivity is interpreted as the transition from an ice-rich upper part of the rock glacier to an ice-poor lower part (Figure 12d). There is no obvious physical explanation, why changes in ice content should produce such a change of the reflectivity pattern. A possible explanation for the change in reflectivity could be a layering within the ice-rich zone, that is, almost pure ice layers may alternate with mixtures of ice and sediments. Furthermore, similar observations were made on the Murtel rock glacier (Maurer and Hauck, 2007), where the transition of an ice-rich to an ice-poor layer was also associated with a change of the GPR reflectivity characteristics.

Within the zone of the active layer (delimited by the white line in Figure 10 and based on a joint interpretation of temperature borehole logs and the low near-surface SRT velocities), there are several resistive and conductive anomalies observed in the ERT tomogram (Figure 10c). High resistivities can be associated with either increased ice content or the presence of air voids. Because the data were acquired in summertime and the active layer shows very low velocities, it must be concluded that these resistive features in the ERT tomogram represent zones of large voids filled with air. The conductive anomalies within the active layer are likely caused by the presence of water. A small pool of liquid water near the weather station and water inflow into borehole F3 during drilling operations support this interpretation

We find generally high resistivities in the zone delimited by the lower boundary of the active layer and the H-GPR constrained transition from ice-rich to ice-poor material (magenta lines in Figure 10) between profile distances 130 and 250 m. Furthermore, the seismic velocities in this region are rather high (3000–4000 m/s). The high resistivities and high seismic velocities are indicative of increased ice content in this zone This is supported by the presence of ice in the geologic borehole logs (Figure 12d; Buchli et al., 2013).

Between profile distances 90 and 130 m, there is a low-resistivity anomaly between the active layer and the bedrock interface (Figure 10c). In the same region, the seismic velocities are of the order of 3000 m/s and the H-GPR data show an increased amount of scattering throughout the entire rock glacier body. On the basis of these observations, we interpret this feature to be a zone having an increased amount of unfrozen water, which is virtually ice-free.

The zone between the ice-rich/ice-poor interface and the basement at profile distances from 130 to 250 m is distinguished by slightly lower resistivities (compared with the overlying zone) and high seismic velocities. The H-GPR and ERT data suggest that there is a decreased amount of ice in this region, but such an interpretation is not fully supported by the SRT results. A possible scenario that would explain all three data sets is fine-grained material filling the interstitial pores after the ice has melted. Grain-filled pores could explain the high seismic velocities.

Figure 11 summarizes the results of the cross profiles P13 (H-GPR), Q2 (SRT), and E1 (ERT). Although P13 is approximately 50 m offset from Q2 and E1 (Figure 1), it is expected to exhibit similar gross structures. As in Figure 10, the inferred bedrock depths (green lines), the ice-rich/ice-poor interface (magenta lines), and the active layer (dashed white lines) have been superimposed.

Small-scale resistive and conductive anomalies within the active layer are again interpreted as zones of large voids and areas of increased moisture. We observe increased resistivities down to the ice-rich/ice-poor interface in the central part of the rock glacier near the crossover points with H5, L1, and E2, which is in turn underlain by lower resistivities in the northern part of the profile. The seismic velocities are of the order of 3000 m/s. We interpret this as a zone of increased ice content, although one would expect slightly higher velocities to support such an interpretation. The underlying low resistivities are again likely due to the presence of water.

At a profile distance of approximately 70 m, there is a conspicuous high-resistivity anomaly that extends to greater depths. In this region, the seismic velocities show decreasingly low values toward the southern end of the profile. To assist our interpretation, we roughly estimated the subsurface composition at that particular lo-

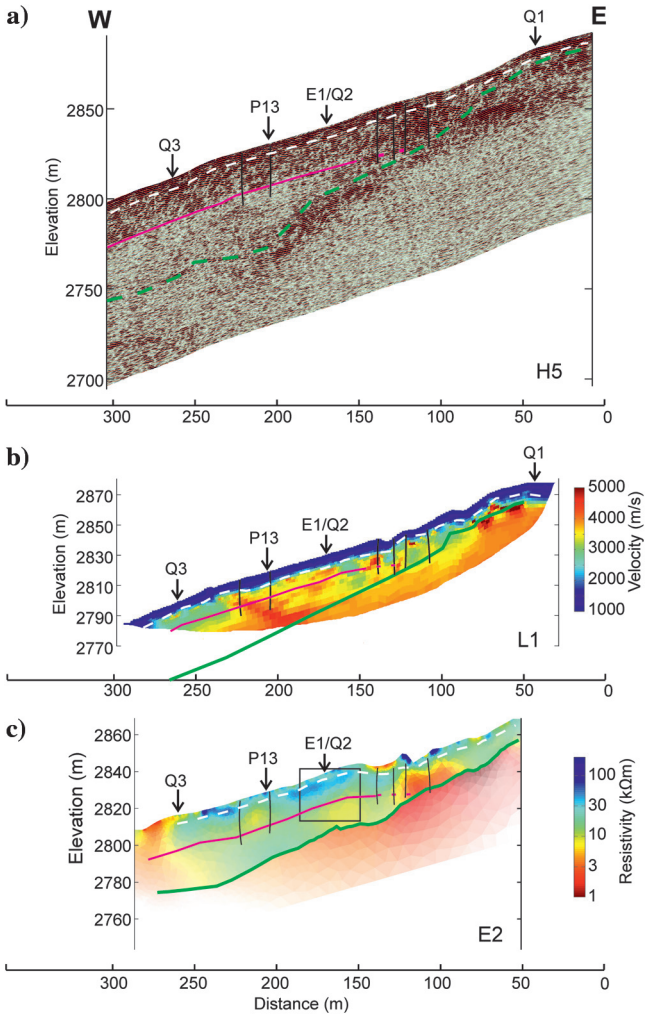

Figure 10. Comparison of longitudinal profiles in the central part of the rock glacier. Portions of the (a) H-GPR profile H5, (b) seismic velocity tomogram L1, and (c) electric resistivity tomogram E2. The dashed white line indicates the depth of the active layer, the magenta line indicates the transition from ice-rich to ice poor permafrost, and the green line indicates the depth of the bedrock. Boreholes are shown in black. Crossing points with profiles in Figure 11 are indicated by arrows at the top of the profiles. For the location of the profiles, see Figure 1.

cation using the four-phase model (Hauck et al., 2011), in which seismic and electric subsurface properties are converted to the four main ingredients of permafrost, namely, rock, ice, water, and air. Porosity was estimated to be 0.3 based on available rock glacier material. Using a seismic velocity of 4500 m/s for the host rock, and values extracted from our tomograms for seismic velocity (1100 m/s) and electric resistivity (100 kΩ), the percentage of ice (4%), water (5%), and air (21%) was estimated. This is a clear indication that the high-resistivity zone is caused by air voids and not by high ice content. Because the uncertainty in porosity reflects directly in the composition estimates, we decided not to extend this approach to the entire rock glacier. The "ice-rich/ice-poor" interface, inferred from the H-GPR data, is also not well developed in this portion of the profile. Based on these observations, it must be concluded that the permafrost has degraded in this part of the rock glacier. The local morphology, bounded to the south by basement rocks and to the north by ice-rich permafrost, forms a preferred drainage path for meltwater and water originating from the small lake near the surface depressions that further enhances permafrost degradation.

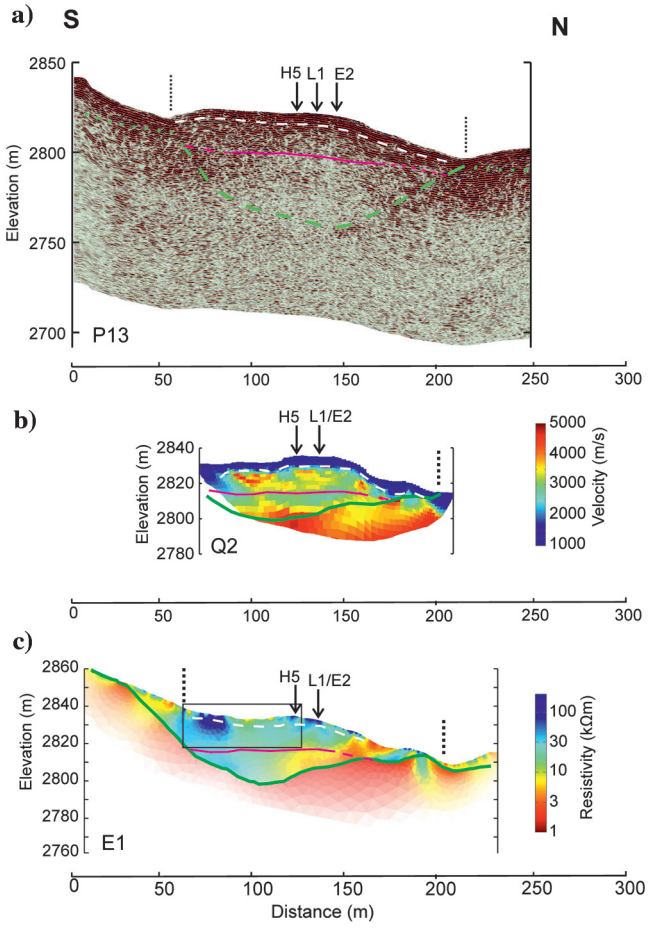

Figure 11. Comparison of cross profiles in the central part of the rock glacier. (a) H-GPR profile P13, (b) seismic velocity tomogram Q2, and (c) electric resistivity tomogram E1. The dashed white line indicates the depth of the active layer, the magenta line indicates the transition from ice-rich to ice poor permafrost, and the green line indicates the depth of the bedrock. The black box shows the location of the 3D ERT survey. Crossing points with profiles in Figure 10 are indicated by arrows at the top of the profiles. For the location of the profiles, see Figure 1. Lateral boundaries of the rock glacier are denoted by vertical dashed black lines.

Based on the profile data alone, it is unclear if the degradation has only occurred locally, or if larger parts of the southern edge have been degraded. Results from the 3D ERT survey clearly support the latter view. The high resistivities extend a few tens of meters to the east, and they can be traced down to the western edge of the 3D ERT survey area. The higher altitudes and the restricted sun exposure due to the surrounding topography seem to have prevented permafrost degradation in the southwestern part of the rock glacier, but it must be assumed that all the ice has disappeared in the southeastern border region. Because large air voids cannot be maintained over longer periods, it is concluded that the degradation has happened recently.

Results from the crosshole tomography offer more insights on small-scale structures. We interpret the crosshole radar tomogram (Figure 12a) jointly with the corresponding structures extracted from seismic profile L1 (Figure 12b) and geoelectric profile E2 (Figure 12c), and we relate them to the stratigraphic and hydrological borehole logs (Figure 12d). These logs are based on the analysis of cuttings from the percussion drilling and are therefore only useful for distinguishing between the main components of the rock glacier material. Near-surface regions with GPR velocities greater than 140 m/μs are indicative of unconsolidated material with either air or loose, fine material in the pores (features a and b in Figure 12). Low seismic velocities in the same areas and their location within the active layer support the interpretation of air-filled voids. Observations at the surface (Figure 2c) also indicate the presence of voids. The high-resistivity zone in Figure 12c, identified as feature a, is also consistent with such an interpretation, but the low resistivities associated with feature b do not seem to be compatible with air-filled voids. A possible explanation is that these low resistivities are caused by the presence of water at the surface or at very shallow depth or voids partially filled with fine material. The smoothing constraints applied to the ERT inversion have likely broadened the vertical extent of the low-resistivity zone. Due to poor ray coverage in the crosshole GPR data near the surface, the reliability of the crosshole tomogram is limited in this region, and it is possible that a very shallow wet zone is therefore missed by GPR crosshole tomography.

Feature c in Figure 12 is characterized by high GPR velocities, high electric resistivities, and high seismic velocities. By analogy with previous interpretations in Figures 10 and 11, we interpret feature c to be a zone of large blocks with interstitial ice. This is supported by subzero temperatures at these depths measured in the boreholes F3 and F4 (Buchli et al., 2013). The lower boundary of feature c is marked with a light brown dashed line in Figure 12. Large surface displacements of 1.7 and 1.4 m/yr were measured at the top of boreholes F4 and F3. The detachment of the thermistor chain at less than a 14 m depth in F4 indicates that most shear deformation occurs across this boundary. Several studies have indicated that large displacements are observed at the base of ice-rich zones (Arenson et al., 2002; Musil et al., 2006). This is a further indication that feature c represents an ice-rich zone.

It is interesting to note that during the past several years, sizable depressions formed between boreholes F2 and F4 (marked as the pink wedge in Figure 12). It is likely that these depressions are related to the lower boundary of feature c, where increased movements have been predicted. (Sub)-horizontal movements at the

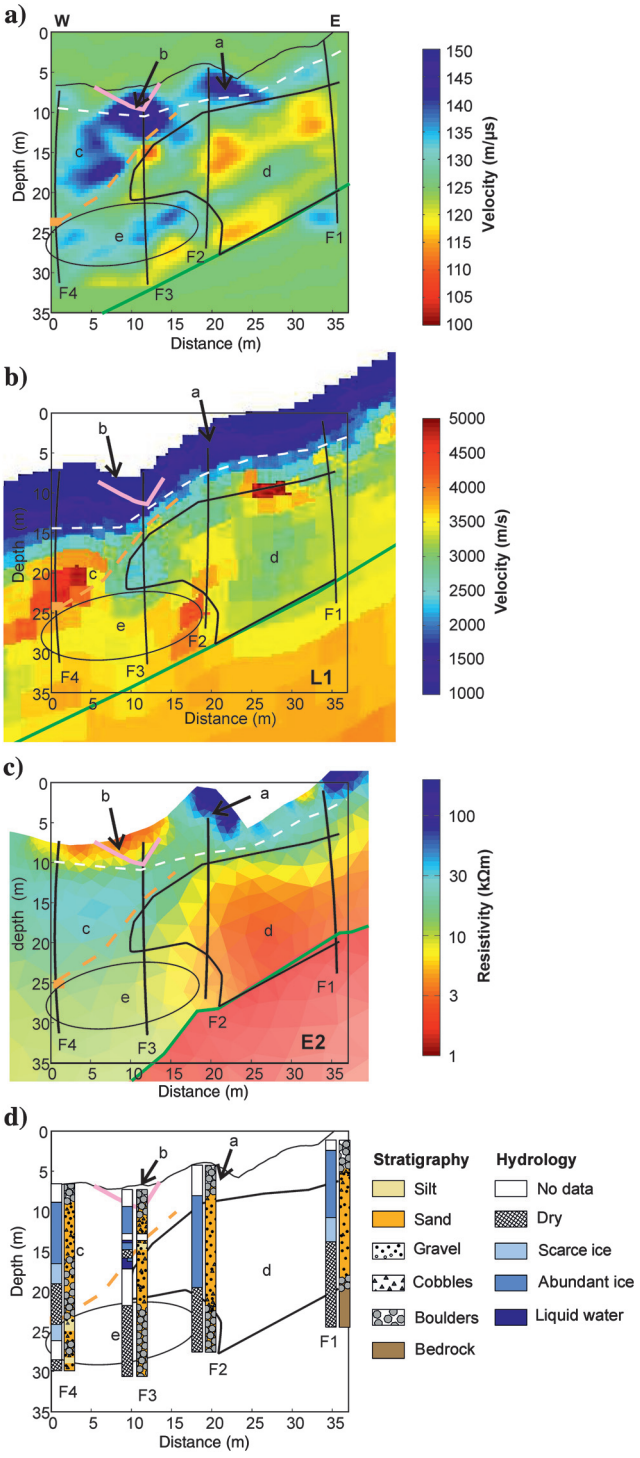

Figure 12. (a) Interpreted radar velocity tomogram for the composite plane F1–F4. The inverted borehole trajectories are shown in black. The location of the ongoing surface depression is shown by the pink wedge. (b) Enlarged extract from seismic tomogram L1. Locations of the boreholes projected on the profile are shown in black. (c) The same ss for panel (b) but for resistivity tomogram E2. (d) Stratigraphic and hydrological logs from boreholes. Letters a-e identify distinct features observed in both sections. The dashed white line marks the depth of the active layer, and the solid green line marks the depth of the basement. The depth of the shear zone is indicated as a solid light brown line in borehole F4. The dashed light brown line gives the interpreted position in the main deformation zone.

lower boundary of feature c, in combination with near-vertical slump structures observed in the depressions, suggest a rotational movement of a larger block in this region. This hypothesis is supported by inclinometer measurements in borehole F5 and eastward tilting of the borehole tubes of F3 and F4 that can be observed at the surface through the rotation of the GPS masts mounted on the concrete blocks around the borehole collars.

Zone d is located below a trough between boreholes F1 and F2 that drains to the north. It is characterized by low and intermediate GPR velocities, low resistivities, and low to intermediate seismic velocities. Borehole data suggest that pore ice is present in this area, and it consists of finer grained material. Partial saturation of this material with water is an explanation for the unexpectedly low GPR velocities and electric resistivities. The electric resistivity and seismic velocity images indicate little structural complexity within zone d, but the crosshole radar tomogram shows a zone

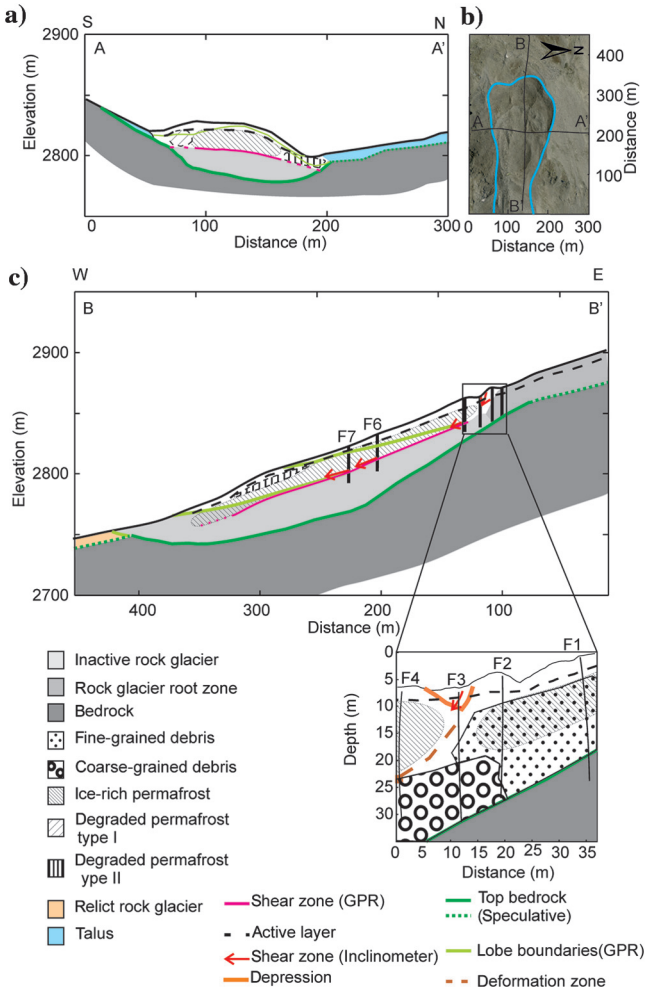

Figure 13. Integrated interpretation of all geophysical measurements on the Furggwanghorn rock glacier. (a) Cross section along the location of H-GPR profile P13. (b) Orthophoto of the rock glacier with demarcation of the boundary in blue and black lines showing the location of the sections (a and c). (c) Longitudinal section along H-GPR profile H5 including a detailed view of the area around the boreholes. See the legend for identification of the individual features.

of intermediate velocities sandwiched by low velocities. Possibly, the low GPR velocity zones in the crosshole tomogram represent preferential flow paths, but considering that they are not imaged by ERT, it can be reasonably inferred that the differences in hydraulic permeability are small. In the deeper part of the rock glacier body between boreholes F3 and F4, we observe high GPR velocities, intermediate resistivities, and intermediate to high seismic velocities (zone e). We interpret this feature as compacted debris including large(r)-grain material.

DISCUSSION

The different data sets presented in this study have yielded a wealth of pertinent information on rock glacier structure. We summarize our main findings in Figure 13. Here, we distinguish between the (1) active layer, (2) bedrock, (3) ice-bearing permafrost, (4) inactive rock glacier (no significant movements), and (5) degraded permafrost, which can be further subdivided into zones where the ice disappeared recently (type I) or some time ago (type II).

Ice-bearing permafrost is found in the central part of the Furggwanghorn rock glacier (Figure 13a), and it is observed between profile distances 120 and 350 m in Figure 13b. It extends from the bottom of the active layer down to maximum depths of approximately 20 m. At the base of this ice-rich body, most of the displacements measured by means of inclinometer readings. In addition, Merz et al. (2015b) identify lobe boundaries within the ice-rich part, where additional movements occur or have occurred (olive-green lines in Figure 13a and 13b). Below the ice-bearing permafrost, there is ice-free rock glacier material. We assume that this part was also frozen at some time.

The low resistivities found at the northern flank and in the lower (western) part of the rock glacier are indicative of degraded type II permafrost. In contrast, the high resistivities along the southern flank must be interpreted as degraded permafrost of type I. Together with the conspicuous formation of depressions, the occurrence of this recently degraded permafrost structures provide clear evidence that permafrost melting seems to have accelerated during the last decade.

The more detailed images obtained from crosshole tomography make it possible to identify small-scale features, and the additional material properties obtained from the GPR velocities allow a distinction to be made between different types of materials in the inactive parts of the rock glacier. Furthermore, they provide additional evidence that the crevicelike depressions observed at the surface are probably slump structures due to melting of ice in zone d (Figure 13c) below the trough.

In addition to offering important new insights on the internal structure of the Furggwanghorn glacier, our study also highlighted the general benefits of multidisciplinary investigations. H-GPR proved to be an excellent tool for delineating the bedrock topography, but alone it was not able to distinguish between permafrost of types I and II. Furthermore, if one would have based the bedrock delineation solely on SRT, this would have likely led to a wrong interpretation in the lower part of the rock glacier because there is insufficient velocity contrast between the bedrock and the zone of grain-filled ice pores. ERT provided critical constraints for identifying ice-rich zones, but without additional information from SRT, some of the high resistivity bodies could have been interpreted incorrectly. In particular, on the basis of ERT alone, one could have likely interpreted the recently degraded permafrost along the southern flank of the rock glacier as a particularly ice-rich zone. If the same conditions were present in a rock glacier that posed a threat to human settlements (which is not the case for the Furggwanghorn rock glacier), then such a different interpretation could have led to catastrophic consequences.

In this contribution, we have performed a rather qualitative integrated interpretation of multimethod geophysical and geotechnical data, which has been based on quantitative measurements. This could be improved by a quantitative analysis of the different physical parameters. A possible option is the four-phase model (Hauck et al., 2011). However, for a reliable conversion of seismic and electric subsurface properties to permafrost composition, dependable estimates of porosity across the rock glacier would be needed. Alternatively, our data sets could form the basis for joint inversions, as proposed by Haber and Oldenburg (1997) and Gallardo and Meju (2007). Such techniques could reveal further structural details that may not be detectable by simple visual inspection of individual method tomograms and reflection images. Finally, it should be emphasized that the tomographic images obtained in this study rather underestimate the heterogeneity of the rock glacier. This is due to the smoothness constraints applied during the inversions. The actual subsurface structures may be even more complex than suggested by our results.

CONCLUSION

Our multidisciplinary investigations on the Furggwanghorn rock glacier agree with evidence that melting of permafrost has accelerated in the last decade at our study site. This may be associated with global warming. Furthermore, our studies confirmed that rock glacier movements are clearly associated with its ice-bearing parts, whereby most of the displacements occur at the lower boundary of the ice-rich zones. Finally, it was demonstrated that rock glaciers can exhibit a complicated 3D pattern of ice-rich and ice-poor zones. Therefore, it is essential that the entire rock glacier body is investigated for assessing the potential of catastrophic failures. This requires methods that sense larger subsurface volumes, and in our view geophysical techniques offer the only viable option to achieve this in a cost-effective manner in association with the ground-truth provided by boreholes and a range of sensors and instruments installed in them for monitoring.

ACKNOWLEDGMENTS

We thank ETH Zurich for the primary funding of this project through CHIRP (grant no. 1-01 09-3). Canton Wallis, Switzerland, through C. Wuilloud, is also thanked for financial contributions. The local Turtmann council is acknowledged for permitting the research team to carry out its field investigations. The authors gratefully acknowledge the essential contributions of the various field crews, GEOSAT SA, Sion, Switzerland for acquiring the helicopter data, and the Landmark Graphics Corporation for providing data processing software through the Landmark University Grant Program. We also thank the two reviewers and the associate editor for their useful comments that improved the quality of the manuscript.

REFERENCES

Arcone, S. A., 2002, Airborne-radar stratigraphy and electrical structure of temperate firn: Bagley Ice Field, Alaska, USA: Journal of Glaciology, **48**, 317–334, doi: 10.3189/172756502781831412.

Arenson, L., M. Hoelzle, and S. Springman, 2002, Borehole deformation measurements and internal structure of some rock glaciers in Switzerland: Permafrost and Periglacial Processes, **13**, 117–135, doi: 10.1002/ppp.414.

Barsch, D., 1996, Rockglaciers indicators for the present and former geoecology in high mountain environments: Springer, Series in Physical Environment.

Berthling, I., B. Etzelmuller, H. Farbrot, K. Isaksen, M. Wale, and R. Odegard, 2008, GPR soundings of rock glaciers on Svalbard, *in* C. Hauck, and C. Kneisel, eds., Applied geophysics in periglacial environments, Cambridge University Press, 172–177.

Boeckli, L., A. Brenning, S. Gruber, and J. Noetzli, 2012, Permafrost distribution in the European Alps: Calculation and evaluation of an index map and summary statistics: The Cryosphere, **6**, 807–820, doi: 10.5194/tc-6-807-2012.

Buchli, T., K. Merz, X. Zhou, W. Kinzelbach, and S. M. Springman, 2013, Characterization and monitoring of the Furggwanghorn rock glacier, Turtmann Valley, Switzerland: Results from 2010 to 2012: Vadose Zone Journal, **12**, doi: 10.2136/vzj2012.0067.

Burger, K. C., J. J. Degenhardt, and J. R. Giardino, 1999, Engineering geomorphology of rock glaciers: Geomorphology, **31**, 93–132, doi: 10.1016/S0169-555X(99)00074-4.

Crosta, G. B., H. Chen, and C. F. Lee, 2004, Replay of the 1987 Val Pola Landslide, Italian Alps: Geomorphology, **60**, 127–146, doi: 10.1016/j.geomorph.2003.07.015.

Florentine, C., M. Skidmore, M. Speece, C. Link, and C. A. Shaw, 2014, Geophysical analysis of transverse ridges and internal structure at Lone Peak Rock Glacier, Big Sky, Montana, USA: Journal of Glaciology, **60**, 453–462, doi: 10.3189/2014JoG13J160.

Gallardo, L. A., and M. A. Meju, 2007, Joint two-dimensional cross-gradient imaging of magnetotelluric and seismic traveltime data for structural and lithological classification: Geophysical Journal International, **169**, 1261–1272, doi: 10.1111/j.1365-246X.2007.03366.x.

Günther, T., and C. Rücker, 2006, A general approach for introducing information into inversion and examples from DC resistivity inversion: Presented at Near Surface 2006 — The 12th European Meeting of Environmental and Engineering Geophysics of the EAGE.

Günther, T., C. Rücker, and K. Spitzer, 2006, Three-dimensional modelling and inversion of DC resistivity data incorporating topography. II: Inversion: Geophysical Journal International, **166**, 506–517, doi: 10.1088/0266-5611/13/1/00610.1111/j.1365-246X.2006.03010.x.

Haber, E., and D. Oldenburg, 1997, Joint inversion: A structural approach: Inverse Problems, **13**, 63–77, doi: 10.1088/0266-5611/13/1/006.

Harris, C., L. U. Arenson, H. H. Christiansen, B. Etzemuller, R. Frauenfelder, S. Gruber, W. Haeberli, C. Hauck, M. Holzle, O. Humlum, K. Isaksen, A. Kaab, M. A. Kern-Lutschg, M. Lehning, N. Matsuoka, J. B. Murton, J. Nozli, M. Phillips, N. Ross, M. Seppala, S. M. Springman, and D. V. Muhll, 2009, Permafrost and climate in Europe: Monitoring and modelling thermal, geomorphological and geotechnical responses: Earth-Science Reviews, **92**, 117–171, doi: 10.1016/j.earscirev.2008.12.002.

Hauck, C., M. Bottcher, and H. Maurer, 2011, A new model for estimating subsurface ice content based on combined electrical and seismic data sets: The Cryosphere, **5**, 453–468, doi: 10.5194/tc-5-453-2011.

Hauck, C., D. Vonder Muhll, and H. Maurer, 2003, Using DC resistivity tomography to detect and characterize mountain permafrost: Geophysical Prospecting, **51**, 273–284, doi: 10.1046/j.1365-2478.2003.00375.x.

Hausmann, H., K. Krainer, E. Brückl, and C. Ullrich, 2012, Internal structure, ice content and dynamics of Ölgrube and Kaiserberg rock glaciers (Ötztal Alps, Austria) determined from geophysical surveys: Austrian Journal of Earth Sciences, **105**, 12–31.

Ikeda, A., 2006, Combination of conventional geophysical methods for sounding the composition of rock glaciers in the Swiss Alps: Permafrost and Periglacial Processes, **17**, 35–48, doi: 10.1002/ppp.550.

Kääb, A., R. Frauenfelder, and I. Roer, 2007, On the response of rockglacier creep to surface temperature increase: Global and Planetary Change, **56**, 172–187, doi: 10.1016/j.gloplacha.2006.07.005.

Kneisel, C., C. Hauck, R. Fortier, and B. Moorman, 2008, Advances in geophysical methods for permafrost investigations: Permafrost and Periglacial Processes, **19**, 157–178, doi: 10.1002/ppp.616.

Krainer, K., L. Mussner, M. Behm, and H. Hausmann, 2012, Multi-disciplinary investigation of an active rock glacier in the Sella Group (Dolomites; Northern Italy): Austrian Journal of Earth Sciences, **105**, 48–62.

Krautblatter, M., S. Verleysdonk, A. Flores-Orozco, and A. Kemna, 2010, Temperature-calibrated imaging of seasonal changes in permafrost rock walls by quantitative electrical resistivity tomography (Zugspitze, German/Austrian Alps): Journal of Geophysical Research: Earth Surface, **115**, F02003, doi:10.1029/2008JF001209.

Krysiecki, J. M., X. Bodin, and P. Schoeneich, 2008, Collapse of the Bérard rock glacier (Southern French Alps), *in* D. L. Kane, and K. M. Hinkel, eds., 9th International Conference on Permafrost: Institute of Northern Engineering, University of Alaska Fairbanks, 153–154.

Lanz, E., H. Maurer, and A. G. Green, 1998, Refraction tomography over a buried waste disposal site: Geophysics, **63**, 1414–1433, doi: 10.1190/1.1444443.

Lehmann, F., and A. G. Green, 2000, Topographic migration of georadar data: Implications for acquisition and processing: Geophysics, **65**, 836–848, doi: 10.1190/1.1444781.

Maurer, H., and A. G. Green, 1997, Potential coordinate mislocations in crosshole tomography: Results from the Grimsel test site, Switzerland: Geophysics, **62**, 1696–1709, doi: 10.1190/1.1444269.

Maurer, H., and C. Hauck, 2007, Geophysical imaging of alpine rock glaciers: Journal of Glaciology, **53**, 110–120, doi: 10.3189/172756507781833893.

Maurer, H., K. Holliger, and D. E. Boerner, 1998, Stochastic regularization: Smoothness or similarity?: Geophysical Research Letters, **25**, 2889–2892, doi: 10.1029/98GL02183.

Merz, K., H. Maurer, T. Buchli, H. Horstmeyer, A. G. Green, and S. M. Springman, 2015a, Evaluation of ground-based and helicopter ground-penetrating radar data acquired across an alpine rock glacier: Permafrost and Periglacial Processes, **26**, 13–27, doi: 10.1002/ppp.1836.

Merz, K., H. R. Maurer, T. Buchli, S. M. Springman, and A. G. Green, 2015b, A new 3D thin-skinned rock glacier model based on helicopter GPR results from the Swiss Alps: Geophysical Research Letters, **42**, 4464–4472, doi: 10.1002/2015GL063951.

Monnier, S., C. Camerlynck, F. Rejiba, C. Kinnard, T. Feuillet, and A. Dhemaied, 2011, Structure and genesis of the Thabor rock glacier (Northern French Alps) determined from morphological and ground-penetrating radar surveys: Geomorphology, **134**, 269–279, doi: 10.1016/j.geomorph.2011.07.004.

Monnier, S., and C. Kinnard, 2013, Internal structure and composition of a rock glacier in the Andes (upper Choapa valley, Chile) using borehole information and ground-penetrating radar: Annals of Glaciology, **54**, 61–72, doi: 10.3189/2013AoG64A107.

Musil, M., H. Maurer, A. G. Green, H. Horstmeyer, F. O. Nitsche, D. V. Muhll, and S. Springman, 2002, Shallow seismic surveying of an Alpine rock glacier: Geophysics, **67**, 1701–1710, doi: 10.1190/1.1527071.

Musil, M., H. Maurer, K. Holliger, and A. G. Green, 2006, Internal structure of an alpine rock glacier based on crosshole georadar traveltimes and amplitudes: Geophysical Prospecting, **54**, 273–285, doi: 10.1111/j.1365-2478.2006.00534.x.

Roer, I., W. Haeberli, M. Avian, V. Kaufmann, R. Delaloye, C. Lambiel, and A. Kääb, 2008, Observations and considerations on destabilizing active rock glaciers in the European Alps: Ninth International Conference on Permafrost **2**, 1505–1510.

Rucker, C., T. Gunther, and K. Spitzer, 2006, Three-dimensional modelling and inversion of DC resistivity data incorporating topography. I: Modelling: Geophysical Journal International, **166**, 495–505, doi: 10.1111/j.1365-246X.2006.03010.x.

Rutishauser, A., H. R. Maurer, and A. Bauder, 2015, Helicopter-borne ground-penetrating radar investigations on temperate alpine glaciers: A comparison of different systems and their abilities for bedrock mapping: Geophysics, **81**, this issue, doi: 10.1190/geo2015-0144.1.

Springman, S. M., L. U. Arenson, Y. Yamamoto, H. Maurer, A. Kos, T. Buchli, and G. Derungs, 2012, Multidisciplinary investigations on three rock glaciers in the Swiss Alps: Legacies and future perspectives: Geografiska Annaler Series A: Physical Geography, **94A**, 215–243.

Swisstopo, 2015, Geological atlas of Switzerland, http://map.geo.admin.ch/?X=115957.59&Y=622234.81&zoom=8&lang=en&topic=ech&bgLayer=voidLayer&layers=ch.swisstopo.geologie-geologischer_atlas, accessed 9 November 2015.

Whalley, W. B., and H. E. Martin, 1992, Rock glaciers: 2. Models and mechanisms: Progress in Physical Geography, **16**, 127–186, doi: 10.1177/030913339201600201.